Available online at www.sciencedirect.com
SCIENCE DIRECT
Journal of Catalysis 228 (2004) 206–217
JOURNAL OF CATALYSIS
www.elsevier.com/locate/jcat

Oxidative steam reforming of methanol on $Ce_{0.9}Cu_{0.1}O_Y$ catalysts prepared by deposition–precipitation, coprecipitation, and complexation–combustion methods

Wenjuan Shan, Zhaochi Feng, Zhonglai Li, Jing Zhang, Wenjie Shen *, Can Li *

State Key Laboratory of Catalysis, Dalian Institute of Chemical Physics, Chinese Academy of Sciences, Dalian 116023, China

Received 4 April 2004; revised 7 July 2004; accepted 8 July 2004

Abstract

The production of hydrogen from oxidative steam reforming of methanol has been tested for $Ce_{0.9}Cu_{0.1}O_Y$ catalysts. The catalysts were prepared by deposition–precipitation (dp), coprecipitation (cp), and complexation–combustion (cc) methods. These catalysts were characterized using BET, TEM, X-ray diffraction (XRD), and Raman spectroscopy. A solid solution was formed in the $Ce_{0.9}Cu_{0.1}O_Y$ prepared by complexation–combustion. The incorporation of Cu atoms into CeO_2 lattice leads to an increase of oxygen vacancy. XPS results indicated that the Cu^+ is the main Cu species for the $Ce_{0.9}Cu_{0.1}O_Y$-cc sample and the synergistic function between Cu^{2+}/Cu^+ and Ce^{4+}/Ce^{3+} occurred in the redox cycle, which is the reason for lower reduction temperatures and improved redox properties as shown in TPR profiles. In the case of the $Ce_{0.9}Cu_{0.1}O_Y$-cp and $Ce_{0.9}Cu_{0.1}O_Y$-dp samples, most CuO dispersed on the CeO_2; the poor interaction between CuO and CeO_2 does not affect redox properties of CeO_2. Methanol conversions higher than 85% with 90% hydrogen yield were obtained for $Ce_{0.9}Cu_{0.1}O_Y$-cc from the oxidative steam reforming of methanol at 240 °C. However, the catalysts prepared by coprecipitation and the deposition–precipitation method showed methanol conversion lower than 30% at 240 °C, and less than 60% even at 360 °C. The high catalytic activity of $Ce_{0.9}Cu_{0.1}O_Y$-cc is mainly related to the formation of solid solution and the improved redox properties.

Keywords: $Ce_{0.9}Cu_{0.1}O_Y$; Solid solution; Redox properties and oxidative stream reforming of methanol

1. Introduction

In recent years, increasing attention has been focused on steam reforming of methanol to produce hydrogen-rich gas as the fuel for low-temperature fuel cells [1–8]. Partial oxidation, steam reforming, and oxidative steam reforming are the primary methods used in the hydrogen production from methanol. Although the high H_2 yield can be obtained from the steam reforming of methanol (SRM), the strong endothermic drawback as well as the relatively slow reaction rate limited its application [9–11]. The partial oxidation of methanol (POM) process offered an exothermic reaction and a higher reaction rate [12]; however, its hydrogen yield was decreased and thermal waste must also be considered. A combination of SRM and POM, the oxidative steam reforming of methanol (OSRM), is the most promising route for the hydrogen production from methanol considering the acceptable hydrogen yield and the possibility of eliminating CO due to the presence of H_2O [13–16]. Furthermore, OSRM has several advantages over SRM and POM for transportation applications due to its autothermal process with idealized reaction stoichiometry,

$$CH_3OH + \tfrac{3}{4}H_2O + \tfrac{1}{8}O_2 = CO_2 + \tfrac{11}{4}H_2 \quad \Delta H^{573\,\mathrm{K}} = 0. \tag{1}$$

These advantages are particularly important because: (1) the autothermal process allows a more rapid response to a change in the power demand and a faster start-up in en-

---

[*] Corresponding authors. Fax: +86 411 84694447.
E-mail addresses: shen98@dicp.ac.cn (W. Shen), canli@dicp.ac.cn (C. Li).

0021-9517/$ – see front matter © 2004 Published by Elsevier Inc.
doi:10.1016/j.jcat.2004.07.010

gine [17], and (2) less heat exchange between incoming reactants and the hot products could simplify the reactor [18].

OSRM has been performed on $CuO/ZnO/Al_2O_3$ catalysts [15,19–21] and the activity of $CuO/ZnO/(ZrO_2)/Al_2O_3$ catalyst has been investigated extensively recently [13,22]. A bifunctional role of copper and ZrO_2 over Cu/ZrO_2-based catalysts for methanol synthesis and decomposition was studied by Fisher and Bell. They suggested that a synergy exists between copper and ZrO_2, in which all the major reaction intermediates are found on ZrO_2, while copper dissociates molecular H_2, which is provided by a spillover mechanism [23–25]. Velu et al. studied the oxidative steam reforming of methanol over CuZnAl(Zr)-oxide catalysts. CuZnZr-oxide catalyst was found to be more effective than CuZnAl-oxide catalyst, indicating that the Zr is a more effective support than Al for Cu and ZnO. The higher catalytic performance of Zr-containing catalysts was attributed to the improved Cu reducibility, higher Cu metal surface area, and dispersion. They also suggested that the reducibility is likely to be an important factor in determining the efficiency of the catalysts for OSRM [21]. Agrell et al. also suggested that the redox properties of the catalyst appear to play a key role in determining the pathway for H_2 production. In particular, the extent of methanol and/or H_2 combustion at differential O_2 conversion is strongly dependent on the ease of copper oxidation in the catalyst [3], but the reverse oxidation of copper is a more difficult process once CuO is reduced [26]. So, a new catalyst with high activity and high redox properties is expected.

In CeO_2, the facile Ce^{4+}/Ce^{3+} redox cycle often leads to a higher oxygen-storage capacity (OSC) with reversible addition and removal of oxygen in the fluorite structure of ceria. The better redox properties than those of CeO_2 alone were obtained by the incorporation of metal ions into the CeO_2 lattice forming $Ce_{1-X}M_XO_Y$ solid solutions, such as Al, Zr, Hf, Si, and La [27–33]. Recently, much effort has been focused on the direct doping of active cations with oxidation states lower than 4+ into the lattice of CeO_2; the purpose is to modify the chemical and physical properties by creating oxygen vacancies inside the parent oxide [34–36]. Surface oxygen and oxygen vacancies are involved in catalytic activity, and an enhanced oxygen mobility will enable the occurrence of redox processes at lower temperatures.

CuO/CeO_2 catalysts have attracted much attention because of their unique catalytic performances associated with environmental concerns [37–42], especially for CO oxidation [43–45], selective oxidation of CO under rich hydrogen [46–48] and water–gas shift reactions [49]. These reactions occur during the oxidative steam reforming of methanol. However, only few investigations were made on the hydrogen production from methanol on CuO/CeO_2 catalysts [50]. Considering the higher redox properties and higher activity of Cu-based catalysts for OSRM, a high catalytic activity is expected for OSRM over CuO/CeO_2 catalyst.

In our previous work, nanosized $Ce_{1-X}Cu_XO_Y$ ($X \leqslant 0.1$) solid solutions are prepared by the complexation–combustion method. The H_2-TPR experiment indicates that the reduction of CeO_2 is not limited to the surface oxygen but extends to the bulk oxygen in the reduction–oxidation processes, which is the reason for the enhanced redox properties in the solid solutions [51]. To further understand the influence of the distribution of Cu species in CuO/CeO_2 catalyst on the redox properties and catalytic activity for OSRM, in this study, the $Ce_{0.9}Cu_{0.1}O_Y$ catalysts were prepared by deposition–precipitation, coprecipitation, and complexation–combustion routes. The catalytic behavior for the oxidative steam reforming of methanol was investigated. It was found that the $Ce_{0.9}Cu_{0.1}O_Y$ prepared by the complexation–combustion method showed not only high catalytic activity but also high H_2 yield. It is seemed that the solid solution structure and the enhanced redox properties have a strong influence on the catalytic behavior.

2. Experimental

2.1. Catalysis preparation

The preparation process affects some properties of ceria-based materials such as the formed phase, particle size, surface area, catalytic activities, and OSC. Therefore, many studies on preparation and modification have been carried out to develop the ceria-based materials of high catalytic activities, OSC, and thermal durability [52–54]. In the present study, deposition–precipitation, coprecipitation, and complexation–combustion methods were selected to obtain catalysis with different Cu species.

Deposition–precipitation is suggested as a preparation method for getting highly dispersed catalysts with strong interaction occurring at the interface of active metal and support [55].

In the coprecipitation process, ideally, a quantitative and simultaneous precipitation of all the cations occurs without segregation of any particular constituents in the precipitates. But, this ideal situation is very rare in most cases. For metal cations Cu^{2+} and Ce^{3+}, it is much more difficult to form coprecipitates with an alkali solution as precipitator because of the considerable difference in the pH value. Therefore, it is reasonable to think that homogeneous coprecipitation at an atomic level is very difficult and most of the resulting precipitate is considered as a mixture of fine particles [56].

In complexation–combustion methods, a solution of citric acid and metal ions is complexed to form a gel precursor with randomly distributed cations. Quickly heating of these precursors at a mild temperature to combust produces mixed oxides that are compositionally homogenous at an atomic level. In this process, the formation of a solid solution with increased oxygen vacancies at a low $Cu/(Ce + Cu)$ ratio is achieved as reported in our previous study [51].

Considering that the solid solutions form only at a low Cu/(Ce + Cu) ratio, the CuO/CeO_2 catalysts with a Cu/(Ce + Cu) ratio of 0.1 were prepared by deposition–precipitation, coprecipitation, and complexation–combustion routes. The preparation process was described in details as follow.

For deposition–precipitation route, CeO_2 was prepared by the precipitation method; i.e., $Ce(NO_3)_3$ aqueous solution was precipitated by dropping the $NaHCO_3$ solution until the pH is 9.0. The obtained solid was washed, dried, and calcinated at 400 °C for 5 h. The resulting powder was CeO_2 and the BET surface area is 116 m^2/g. A 1 M $NaHCO_3$ solution was dropped to a suspended solution containing $Cu(NO_3)_2$ and CeO_2 powder. The pH value of the mixture was maintained at 8.5 for 2 h. The resulting solid was washed with warm distilled water (70 °C), vacuum-dried for 5 h, and calcinated at 450 °C for 5 h. It was $Ce_{0.9}Cu_{0.1}O_Y$-dp.

For the coprecipitation route, 0.15 M $NaHCO_3$ aqueous solution was added to the premixed aqueous solution of $Ce(NO_3)_3 \cdot 6H_2O$ and $Cu(NO_3)_2 \cdot 3H_2O$ at 70 °C until the pH value of the mixture reached 8.5. After aging for 2 h, the precipitate was filtered off, washed with warm distilled water (70 °C), vacuum-dried for 5 h, and finally calcinated at 450 °C for 5 h. It was named as $Ce_{0.9}Cu_{0.1}O_Y$-cp.

For the complexation–combustion process, the $Ce(NO_3)_3 \cdot 6H_2O$ and $Cu(NO_3)_2 \cdot 3H_2O$ were dissolved in deionized water in such a manner to give a solution of 1.0 M. Citric acid was added with 1.2 times molar amounts to the premixed nitrate solution of cerium and copper. The solution temperature was kept at 70 °C for 2 h. In the process, the mixture color changed from blue to green and the pH value was about 1.0. Once the gel formed, the temperature was elevated to 150 °C quickly. The gel foamed with production of nitrogen oxide vapors and burnt with sparks. A solid product was obtained after the sparks were extinguished. Then the sample powder was calcined at 450 °C for 5 h in air. The sample thus obtained is referred to as $Ce_{0.9}Cu_{0.1}O_Y$-cc.

2.2. Characterization

The specific area of the samples was obtained at 77 K using a Micromeritics ASAP 2010. Prior to measuring, the samples were pretreated in vacuo at 300 °C for 2 h.

TEM investigations were carried out using a JEOL JEM-2000EX microscope operating at 100 kV.

X-ray powder diffraction (XRD) patterns were recorded on a Rigaku Rotaflex (RU-200B) powder diffractometer using nickel-filtered Cu$K\alpha$ radiation. The mean crystallite size of the cubic phase was calculated from the Scherrer equation, where the Scherrer constant (particle shape factor) was taken as 0.89. The lattice parameters were calculated according to the Cohen procedure [57].

Temperature-programmed reduction (TPR) was conducted using a conventional apparatus equipped with a TCD detector. A molecular sieve trap was placed before the detector to adsorb the produced water. TPR was performed by heating the samples (50 mg) at 10 °C/min to 500 °C in a 5% H_2–N_2 mixture flowing at 40 ml/min. Then, the samples were further reoxidized at 300 °C for 2 h with a 20% O_2/N_2 mixture. Thereafter, temperature-programmed reduction measurements were performed again by cooling the samples down to room temperature under N_2 flow.

X-ray photoelectron spectra (XPS) were acquired on a VG ESCALAB MK-2 spectrometer using Al$K\alpha$ radiation (1486.6 eV). The aluminum anode was operated at an accelerating voltage of 13 kV. The powder sample was pressed to a wafer with a diameter about 13 mm. Base pressure in the analysis chamber was maintained in the range of 2×10^{-8} Pa. In the reduction–oxidation processes, the sample was in the pretreatment chamber and was pretreated by H_2 or air (30 ml/min) for 2 h at 300 °C, respectively. When the sample was cooled under He, the chamber was vacuumized, and the XPS experiment was performed.

Visible Raman spectra were recorded on a Jobin-Yvon U1000 scanning with a 532-nm single-frequency laser. Samples were mounted in a spinning holder to avoid thermal damage during the spectrum scanning, which usually takes about 5 min. The Raman signal was collected with a 90° geometry. The spectra of all samples were recorded at room temperature.

UV Raman spectra were recorded on a homemade UV Raman spectrograph, which has four key parts: a UV cw laser, a Spex 1877d triplemate spectrograph, a CCD detector, and an optical collection system. A line at 325 nm from a He–Cd laser with an output of 25 mW is used for excitation source of the UV Raman spectroscopy. The laser power measured at the samples was below 4.0 mW for 325 nm radiation.

2.3. Catalytic activity

The oxidative steam reforming of methanol reaction was performed by using a continuous-flow quartz fixed-bed reactor ($\phi = 6$ mm) in the temperature range from 240 to 360 °C under atmospheric pressure. A 300 mg catalyst (40–60 mash) was loaded into the reactor. The catalyst was pretreated with 20% O_2/N_2 at 300 °C for 2 h. After cooling down to the reaction temperatures under He, the reaction feed containing 20 vol% methanol, 26 vol% water, and 6 vol% oxygen balanced by helium was introduced with a total gas flow rate of 100 ml/min. The outlet gaseous mixture was analyzed using an on-line gas chromatograph (Varian GC3800) equipped with TCD and FID detectors. A Hayerry D column (5 m) and a 13 X column (2 m) were used to detect the gaseous products such as H_2, CO_2, CO, O_2, and N_2 by TCD. A PE-20000 column (25 m) was used to analyze the liquid products such as methanol, formic acid, formaldehyde, and dimethyl ether by FID. The conversion of CH_3OH was calculated by

$$\text{Conversion of } CH_3OH = 1 - \frac{CH_3OH_{out}\ \text{vol\%}}{\text{Total carbon vol\%}}. \tag{2}$$

The selectivity of CO_2 can be defined as the molar ratio of CO_2 produced to that of CO_2 and CO,

$$\text{selectivity of } CO_2 = \frac{CO_2 \text{ vol\%}}{CO_2 \text{ vol\%} + CO \text{ vol\%}}. \tag{3}$$

The yield of hydrogen was defined as the molar ration of hydrogen produced to the theoretic value according the reaction: $CH_3OH + (1-2\delta)H_2O + \delta O_2 = (3-2\delta)H_2 + CO_2$ in which the δ is 0.3,

$$\text{Yield of } H_2 = \frac{\text{mole } H_2}{(3-2\delta)H_2 \times \text{con.\% of } CH_3OH}. \tag{4}$$

3. Results and discussion

3.1. The structural studies of $Ce_{0.9}Cu_{0.1}O_Y$ catalysts

Table 1 lists the surface area, the pore parameter, and the particle sizes of the $Ce_{0.9}Cu_{0.1}O_Y$ catalysts. For the samples calcinated at 450 °C, the largest BET area was observed for $Ce_{0.9}Cu_{0.1}O_Y$-cp. For the $Ce_{0.9}Cu_{0.1}O_Y$-dp, the BET area and pore volume were only half of those in $Ce_{0.9}Cu_{0.1}O_Y$-cp, but similar particle sizes were observed. The $Ce_{0.9}Cu_{0.1}O_Y$-cc has a similar BET area to that of $Ce_{0.9}Cu_{0.1}O_Y$-dp and its pore parameter is much higher than that of $Ce_{0.9}Cu_{0.1}O_Y$-dp. When the effect of calcination temperature is considered, it can be seen that the $Ce_{0.9}Cu_{0.1}O_Y$-cc catalyst calcinated at 850 °C presents a surface area decreases by 10 times, compared to the sample calcinated at 450 °C. The corresponding changes in the pore volume also greatly decreased from 0.1 to 0.009 ml/g. Accordingly, the particle size increased from 6.1 to 25.4 nm.

Table 1
BET surface areas, pore parameter particle size, and lattice parameter of $Ce_{0.9}Cu_{0.1}O_Y$ catalysts

Samples	BET (m^2/g)	Pore volume (ml/g) $\times 10^{-2}$	Particle size (nm)	Lattice parameter a (Å)
dp-450	46.7	4.2	9.1	5.4140
cp-450	92.2	7.2	8.2	5.4274
cc-450	48.9	10.2	6.1	5.4203
cc-650	29.8	8.8	11.6	5.4482
cc-850	4.0	0.9	25.4	5.4651
dp-850	–	–	–	5.4808
cp-850	–	–	–	5.3875

The TEM images of $Ce_{0.9}Cu_{0.1}O_Y$-450 are given in Fig. 1. In all the cases, Cu particles could not be distinguished from cerium in the electron microscopy images due to the lower copper atomic weight and the poor contrast. However, it can be observed that the morphology of the $Ce_{0.9}Cu_{0.1}O_Y$ catalysts still depended on the preparation methods. The TEM image of the $Ce_{0.9}Cu_{0.1}O_Y$-cc is somewhat similar to the pure CeO_2, as reported by Bera et al. [34], which may be an indication that the Cu species incorporated into the CeO_2 lattice by the complexation–combustion route.

Fig. 2 shows the XRD patterns of $Ce_{0.9}Cu_{0.1}O_Y$ catalysts prepared by different methods. No CuO diffraction peaks presented for all the samples due to the low Cu content. The average particle sizes of cerium oxide were calculated to be 6.1, 8.2, and 9.1 nm, respectively, for the samples calcination at 450 °C prepared by complexation–combustion, coprecipitation, and deposition–precipitation methods. With increasing calcination temperature from 450 to 850 °C, a sharp increase in the intensity of the peaks due to better crystallization of cerium oxide was noted. Another observation to be noted from XRD measurements is that there are no extra peaks due to compounds or mixed phases between CeO_2 and CuO.

The position of cubic CeO_2 diffraction peaks shifted strongly depended on the preparation routes. In the case of the cubic CeO_2 (111) diffraction peak, a lower 2θ value was observed in the $Ce_{0.9}Cu_{0.1}O_Y$-cc and $Ce_{0.9}Cu_{0.1}O_Y$-cp in contrast with the $Ce_{0.9}Cu_{0.1}O_Y$-dp sample. A noticeable shift in the positions of the peak toward lower 2θ values could be taken as an indication of lattice expansion as shown in Table 1. Note that the Cu^{2+} ionic radius (0.72 Å) is

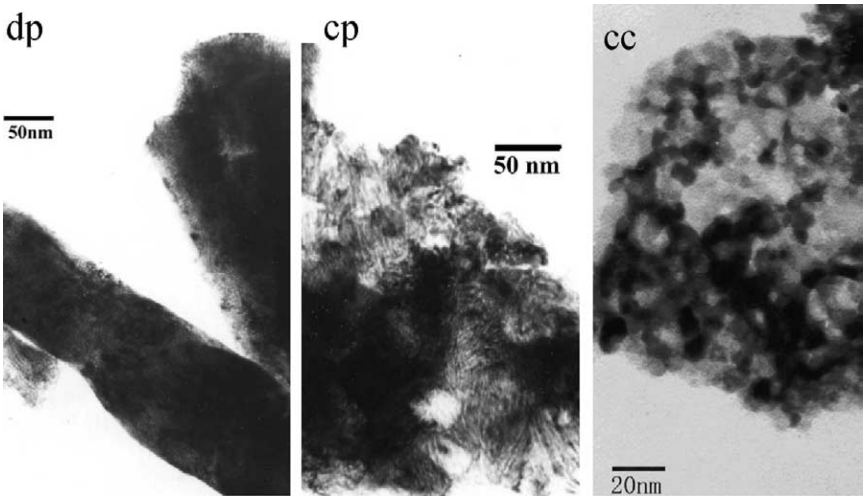

Fig. 1. TEM images of $Ce_{0.9}Cu_{0.1}O_Y$-450 catalysts prepared by different methods.

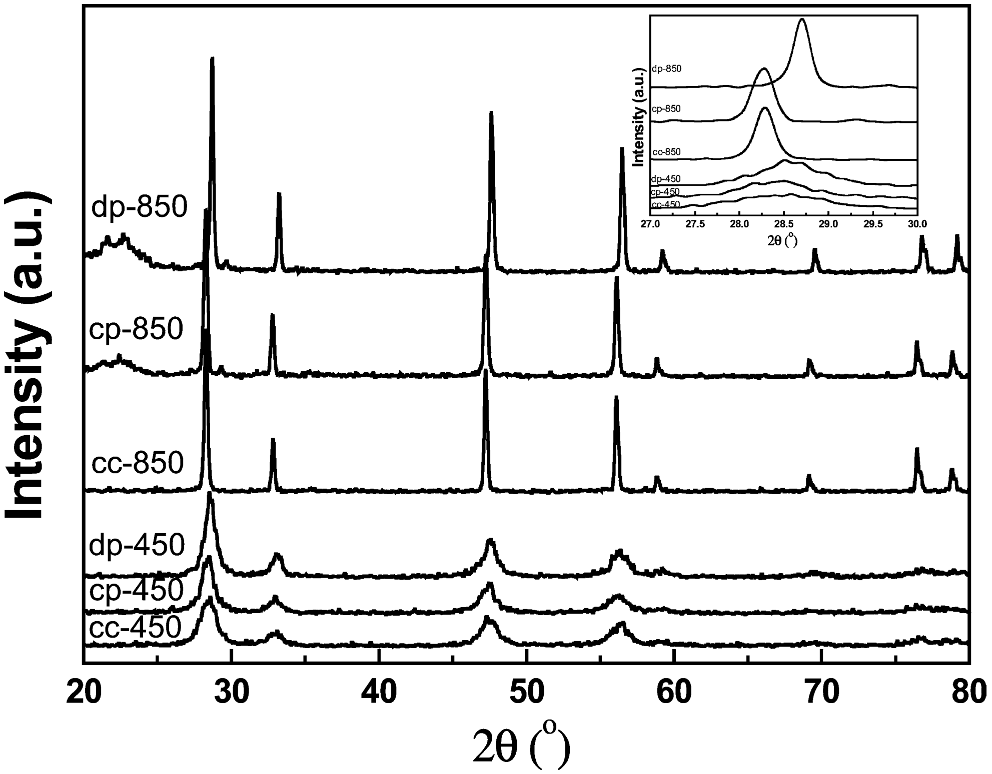

Fig. 2. XRD patterns of $Ce_{0.9}Cu_{0.1}O_Y$-450 prepared by different methods.

smaller than that of the Ce^{4+} cation (0.92 Å). The shift originates from the presence of Ce^{3+} ions in the CeO_2 lattice. Because of the large difference between the ionic dimensions of the Ce^{4+} (0.92 Å) and Ce^{3+} (1.03 Å) ions, the lattice expansion of CeO_2 can be expected. It was suggested that the formation of substoichiometric fluorite-structured CeO_{2-x} is related to the thermal treatments [58]. Whereas, in this case, the samples were calcinated at the same temperature, so the other possibility that could be responsible for the lattice expansion is the formation of oxygen vacancies due to the dopant-induced defects in solid solution structure. For the cc and cp methods, the catalysts were prepared from liquid precursors; Cu^{2+} ion is possible to incorporate into the CeO_2 lattice to form a solid solution. As a result, a depletion of oxygen occurs, leading to the formation of substoichiometric fluorite-structured CeO_{2-x} with oxygen vacancies.

In contrast to XRD results, which yield information related to the cation sublattice, Raman spectroscopy of these fluorite type oxide structures is dominated by oxygen lattice vibrations. It is sensitive to the crystal symmetry, thus being a potential tool to obtain additional structural information.

Fig. 3 compares the visible Raman spectroscopies between pure CeO_2 and $Ce_{0.9}Cu_{0.1}O_Y$ catalysts calcinated at 450 °C. A sharp peak at 462 cm^{-1} ascribed to cubic CeO_2 was observed. The peak shifted from 462 to 452 cm^{-1} in the $Ce_{0.9}Cu_{0.1}O_Y$-dp and 443 cm^{-1} in both the $Ce_{0.9}Cu_{0.1}O_Y$-cc and $Ce_{0.9}Cu_{0.1}O_Y$-cp catalysts. It was broader and weaker than that in CeO_2. This shift may imply that changes in the lattice parameter with particle size have occurred, as it was previously reported that a change of the particle size of CeO_2 from 6 nm to 5 μm led to a shift in peak position about 10 cm^{-1} [59]. But, in the present study, no change

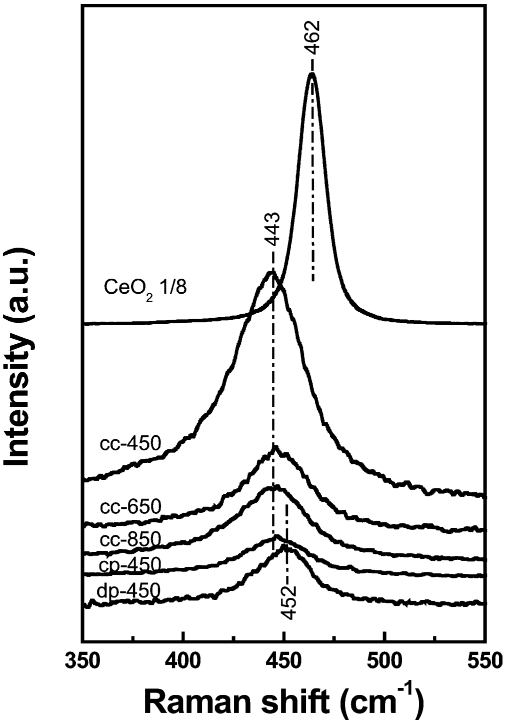

Fig. 3. Raman spectra of $Ce_{0.9}Cu_{0.1}O_Y$ catalysts excited by 532-nm laser line.

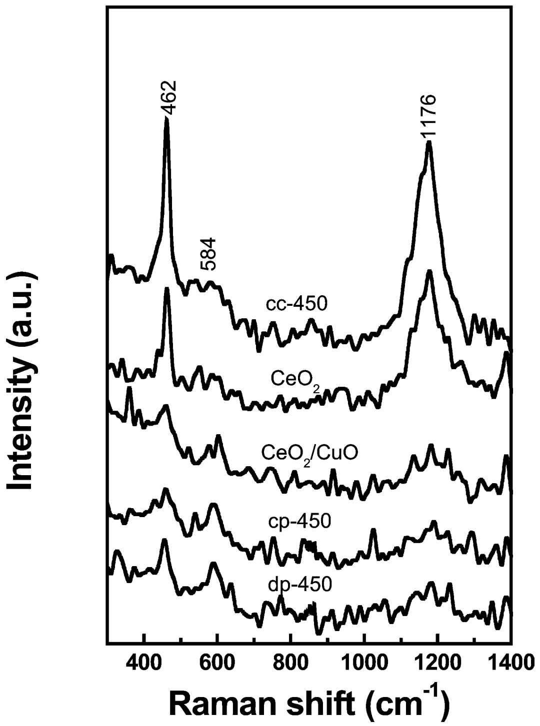

Fig. 4. Raman spectra of $Ce_{0.9}Cu_{0.1}O_Y$ catalysts excited by 325-nm laser line.

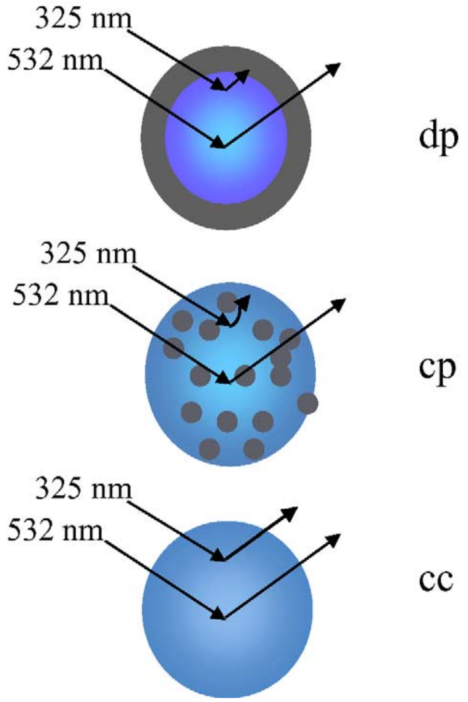

Fig. 5. Schematic description of the structural information of $Ce_{0.9}Cu_{0.1}O_Y$ catalysts obtained from XRD and Raman spectroscopy.

in the peak position was observed with increasing of the particle size from 6.1 to 25.4 nm when the calcination temperature changed from 450 to 850 °C. The most probable interpretation of shifting and broadening is the presence of oxygen vacancies, corresponding to stoichiometry $CeO_{2-\delta}$, which was related to a change of CeO_2 environment in the presence of copper due to the formation of solid solutions. So it can be suggested that the Cu–Ce–O formed a solid solution in $Ce_{0.9}Cu_{0.1}O_Y$ prepared by coprecipitation and complexation–combustion methods.

Fig. 4 shows the UV Raman spectra recorded by using a laser at 325 nm as the excitation source. A broad band with relatively high intensity was observed at 462 cm^{-1} for cubic CeO_2 in the $Ce_{0.9}Cu_{0.1}O_Y$-cc solid solution together with two bands at about 584 and 1176 cm^{-1} which is not normally observed by Raman spectra. However, the presence of some defects can involve relaxation of the selection rules. In particular, these bands have been linked to oxygen vacancies in the CeO_2 lattice [60]. A weak peak between 550 and 600 cm^{-1} and a weaker second-order peak at about 1184 cm^{-1} (relative to the 462 cm^{-1}) were attributed to the presence of CeO_2 defects [59]. However, in the present study, a weak peak at 584 cm^{-1} and a peak at 1176 cm^{-1} with a similar intensity as the peak at 462 cm^{-1} were observed. The increasing peak intensity at 1176 cm^{-1} might be due to the resonance Raman enhancement. Therefore, the bands at 584 and 1176 cm^{-1} can be assigned to the defects of the ceria fluorite structure. Compared with CeO_2, the physical mixture ($CeO_2/CuO = 1/1$) sample showed the reduced Raman modes due to the strong adsorption of CuO in the region. A similar phenomenon was observed for $Ce_{0.9}Cu_{0.1}O_Y$-cp and $Ce_{0.9}Cu_{0.1}O_Y$-dp catalysts, which were produced by some CuO dispersed on CeO_2, while the enhanced Raman modes were observed in the $Ce_{0.9}Cu_{0.1}O_Y$-cc solid solution that increased the defects by creating more oxygen vacancies. This fact also provides direct evidences that the Cu^{2+} ions incorporate in CeO_2 lattice to a form solid solution, instead of dispersing on CeO_2 surface in $Ce_{0.9}Cu_{0.1}O_Y$-cc.

Another interesting phenomenon was observed; i.e., in the case of $Ce_{0.9}Cu_{0.1}O_Y$, the 462 cm^{-1} band is shifted for visible spectra, while no shift is observed for UV spectra. In our previous study with UV–vis spectroscopies of CeO_2 and $Ce_{0.9}Cu_{0.1}O_Y$ samples, two broad bands at 260 and 367 nm are attributed to CeO_2. In the $Ce_{0.9}Cu_{0.1}O_Y$ solid solution, the adsorption edge at 367 nm is blue-shifted and weakened, and a broad and weak band ranging from 400 to 600 nm was also observed [51]. So, the visible Raman spectra showed the bulk information about the catalysts, While the UV Raman spectra provided much more surface information. On the surface, the structure of CeO_2 with oxygen vacancies plays an important role. Although some CuO dispersed on the CeO_2 surface reduced the peak intensity, it showed no influence on the peak position. In the bulk, the Ce–O band was strongly modified by the presence of Cu ions in the lattice, which is the reason for shifting the visible spectra.

For the different preparation methods, a schematic description of the Cu atoms in $Ce_{0.9}Cu_{0.1}O_Y$ catalysts as deduced from XRD and Raman spectra is shown in Fig. 5. Generally speaking, Raman scattering comes from both the surface and the bulk of a solid sample. But the signal from the bulk is attenuated when the sample strongly absorbs the excitation laser light and the scattering light. In the case of $Ce_{0.9}Cu_{0.1}O_Y$-dp, most CuO dispersed on the surface of CeO_2 and the strong adsorption of CuO leading to Raman scattering signal from CeO_2 attenuated in Raman spectra using a 325-nm laser line. A similar phenomenon was observed for $Ce_{0.9}Cu_{0.1}O_Y$-cp in which highly dispersed CuO and solid solution coexisted as confirmed by XRD and Raman results. Whereas Cu^{2+} incorporated into CeO_2 lattice to form solid solution in $Ce_{0.9}Cu_{0.1}O_Y$-cc, which enhanced the Raman scattering peaks instead of reducing them. In the Raman spectra excited by a 532-nm laser line, the shifted band at about 462 cm^{-1} was observed for all $Ce_{0.9}Cu_{0.1}O_Y$ catalysts because there is usually no electronic absorption in the visible region for most samples. The shift degree depends on the environmental change of CeO_2.

3.2. *Redox properties of $Ce_{0.9}Cu_{0.1}O_Y$ catalysts*

Fig. 6 shows the preliminary TPR profiles of the $Ce_{0.9}Cu_{0.1}O_Y$ catalysts prepared by different methods. It can be seen that the reduction property strongly depended on the preparation route. For the $Ce_{0.9}Cu_{0.1}O_Y$-cc catalyst, two reduction peaks centered at 190 and 226 °C were observed. The $Ce_{0.9}Cu_{0.1}O_Y$-cp catalyst showed a peak at 265 °C with a low temperature shoulder peaks (about 230 °C). Two reduction peaks were also observed in the TPR profile of $Ce_{0.9}Cu_{0.1}O_Y$-dp, but the reduction temperatures were higher than those of $Ce_{0.9}Cu_{0.1}O_Y$-cc catalyst, which were at 245 and 270 °C, respectively.

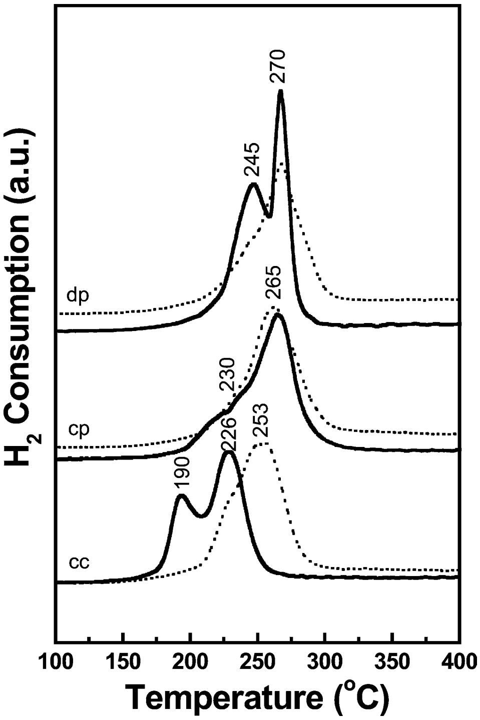

Fig. 6. TPR profiles of $Ce_{0.9}Cu_{0.1}O_Y$-450 prepared by different methods. —: Fresh samples; ···: the samples after being reoxidated at 300 °C.

Based on the structure results, it was suggested that the solid solution formed in $Ce_{0.9}Cu_{0.1}O_Y$-cc. The incorporation of lower valent Cu species into the ceria lattice introduced structural defects; however, the cerium sublattice is not strongly perturbed by the defects, which instead cause the formation of a defective oxygen sublattice. The defect is not localized in one single oxygen site but instead extends to additional surrounding oxygen positions. So, many oxygen vacancies were generated with the formation of the solid solutions. The oxygen vacancies of $Ce_{0.9}Cu_{0.1}O_Y$ solid solution-adsorbed oxygen from surroundings can be reduced at lower temperatures. Therefore, the peak at 190 °C can be ascribed to the reduction of these oxygen species. Since, the formation of solid solution reduced the reduction temperature of CuO and promoted the reduction of CeO_2, the peak at 226 °C was the reduction of CuO and part reduction of CeO_2. For the $Ce_{0.9}Cu_{0.1}O_Y$ catalysts prepared by coprecipitation and deposition–precipitation routes, the main peaks at 265 and 270 °C can be ascribed to the reduction of Cu^{2+} species on the surface of CeO_2. While the shoulder peaks at 230 °C in $Ce_{0.9}Cu_{0.1}O_Y$-cp and at 245 °C in $Ce_{0.9}Cu_{0.1}O_Y$-dp can be attributed to the reduction of CuO species at the interface between CuO and CeO_2 where the interaction takes place.

The TPR profiles of $Ce_{0.9}Cu_{0.1}O_Y$ catalysts reoxidized at 300 °C after the preliminary measurement are also compared in Fig. 6 with the dotted curves. It can be seen that the reduction peaks shifted to high temperatures and the two peaks at 190 and 226 °C overlapped to one peak centered at 253 °C for $Ce_{0.9}Cu_{0.1}O_Y$-cc. This phenomenon demonstrated that copper and cerium atoms redistributed because new sites of low energy became available during reduction–oxidation processes [61]. However, the reduction property showed no difference between fresh and reoxidized samples for the $Ce_{0.9}Cu_{0.1}O_Y$-cp. Similar TPR plots and H_2 consumption were observed. The peaks at 245 and 270 °C became weak after reoxidation and the obvious poor reproducibility was observed for the $Ce_{0.9}Cu_{0.1}O_Y$-dp.

To further understand the difference in the redox properties, a quantitative analysis was performed on the $Ce_{0.9}Cu_{0.1}O_Y$ samples prepared by the three methods. Fig. 7 plots the H_2 consumption ratio of the reoxidation sample to the corresponding fresh sample as a function of reoxidation temperatures. It can be seen that the H_2 consumption ratio is 0.97, 0.78 and 0.88, respectively, for the $Ce_{0.9}Cu_{0.1}O_Y$-cc, $Ce_{0.9}Cu_{0.1}O_Y$-cp, and $Ce_{0.9}Cu_{0.1}O_Y$-dp samples, when they were reoxidized at 100 °C for 2 h after the preliminary reduction up to 500 °C. A decreased H_2 consumption ratio with a higher reoxidation temperature was shown for the $Ce_{0.9}Cu_{0.1}O_Y$-dp sample, it reduced from 0.88 to 0.84. When increasing the reoxidation temperature to 200 °C, an increased trend was observed for $Ce_{0.9}Cu_{0.1}O_Y$-cp and $Ce_{0.9}Cu_{0.1}O_Y$-cc. The ratio is 1.01 and 1.10, respectively, and the numbers almost have no change at 300 °C. These

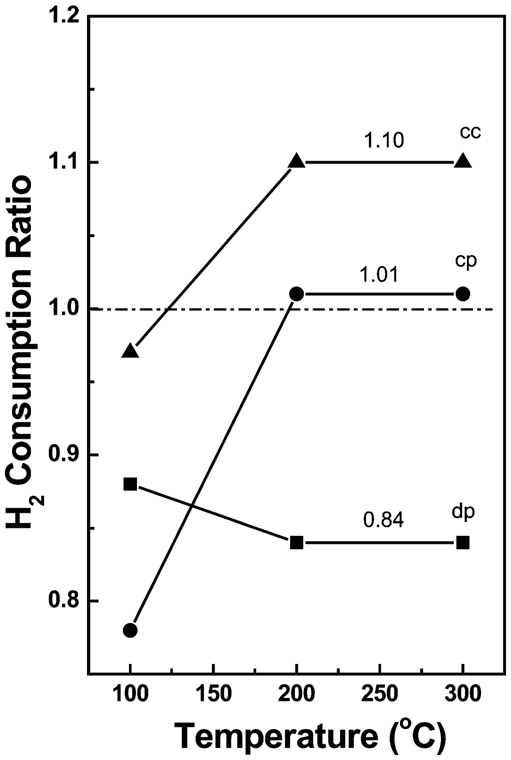

Fig. 7. H_2 consumption ratio for the $Ce_{0.9}Cu_{0.1}O_Y$ catalysts as function of reoxidation temperatures.

results can be explained by the different Cu atom dispersions. Since the CuO does not have complete reproducibility after being reduced [26], the H_2 consumption ratio decreases with the increased redox cycle even at a gradually elevated temperature for the $Ce_{0.9}Cu_{0.1}O_Y$-dp catalysts. In $Ce_{0.9}Cu_{0.1}O_Y$-cc, the enhanced redox properties was observed since the formation of solid solution with oxygen vacancies not only reduces the reduction temperature but also promotes the mobility of bulk oxygen as explained in detail in our previous study [51]. In the case of $Ce_{0.9}Cu_{0.1}O_Y$-cp, the highly dispersed CuO shows low reproducibility; furthermore, it covers some surface oxygen vacancies which play an important role in the redox process. So the redox properties show no further improvement.

3.3. The chemical state study of Ce and Cu in the $Ce_{0.9}Cu_{0.1}O_Y$ catalysts in the redox process

In order to gain information about the chemical state of copper and cerium on the catalyst surface, X-ray photoelectron spectra were collected for $Ce_{0.9}Cu_{0.1}O_Y$ catalysts after exposure to various conditions, viz. (a) fresh after calcination in air, (b) after reduction in H_2 at 300 °C for 2 h, and (c) reoxidation in air at 300 °C for 4 h following (b).

Fig. 8. shows the Ce3d XPS spectra of the $Ce_{0.9}Cu_{0.1}O_Y$ prepared by different methods. The six peaks (u, u″, u″′, v, v″, v″′) are associated with the four-valent Ce $4f^0$ initial state of CeO_2 in Fig. 8a. The two peaks (u′, v′) in Fig. 8b are characteristic of the Ce $4f^1$ initial state and correspond to trivalent cerium. From Fig. 8a, it can be seen that the peaks (u′, v′) ascribed to the Ce^{3+} appeared for the fresh $Ce_{0.9}Cu_{0.1}O_Y$-cp, leading to the broadening and shifting of the $Ce3d_{5/2}$ (v) peak. These peaks were observed clearly for the reduced $Ce_{0.9}Cu_{0.1}O_Y$ as shown in Fig. 8b, which suggested that the Ce^{4+} was reduced by H_2 at 300 °C. The reduced Ce^{3+} can be reoxidized in air at 300 °C as shown in Fig. 8c.

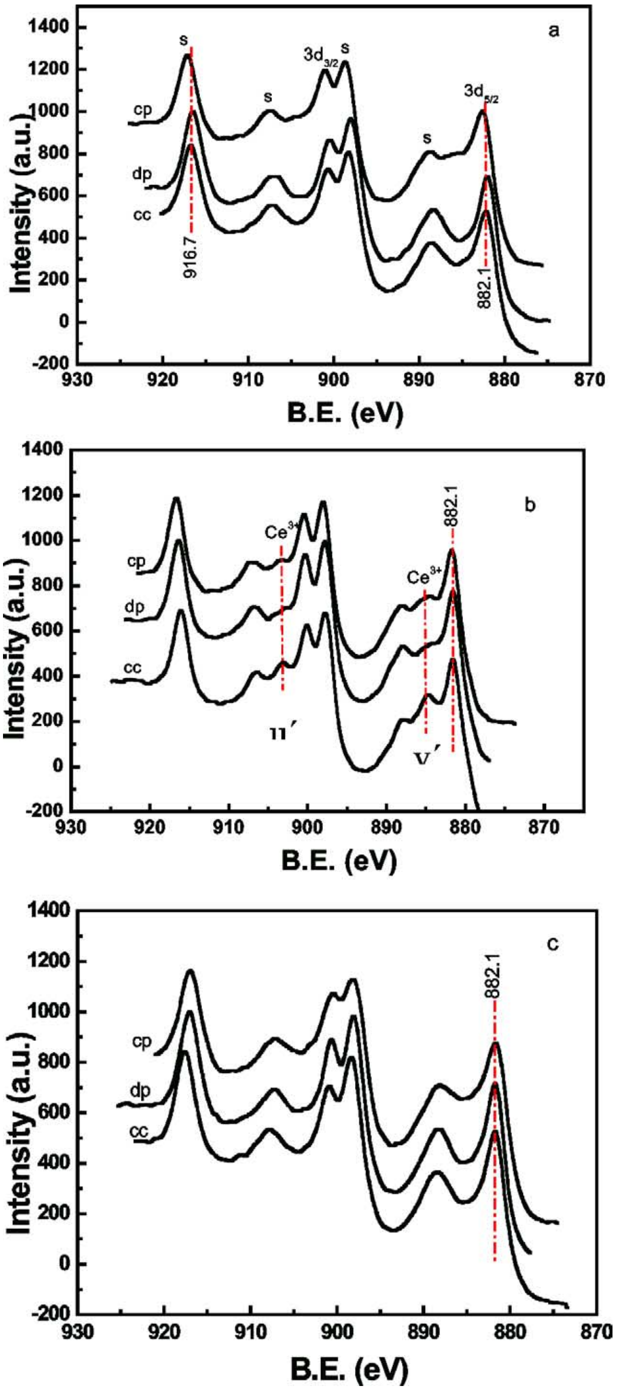

Fig. 8. XPS spectra of Ce3d of $Ce_{0.9}Cu_{0.1}O_Y$ samples, (a) for fresh samples, (b) for the sample reduced by H_2 at 300 °C for 2 h, (c) for reoxidation in air at 300 °C for 4 h following (b).

Table 2
Oxidation states of $Ce_{0.9}Cu_{0.1}O_Y$ under different conditions, as determined from XPS spectra

	Samples	$Cu2p^{3/2}$ I_{sat}/I_{pp} (%) [64]	$Ce3d^{5/2}$ Ce(916.7)/Ce(tot) (%) [62]
	CuO	50–60	
	CeO_2		13.7
cc	Fresh	8.7	10.2
	H_2-300 °C	0.1	8.9
	RO-300 °C	11	10.4
cp	Fresh	13.4	9.2
	H_2-300 °C	2.6	9.1
	RO-300 °C	16.3	9.7
dp	Fresh	9.7	11.0
	H_2-300 °C	8.0	9.6
	RO-300 °C	10.5	11.3

The proportion of Ce^{4+} and Ce^{3+} is difficult to obtain due to the very similar energies of the 4f and orbital ligand valence level. The peak located at BE $\approx$ 916.7 eV appears to be typical of Ce^{4+} and absent for Ce^{3+}, and consequently decreases upon reduction, and thus used frequently for this purpose. The percentage of the total integrated spectrum intensity lying within this peak in pure, nonreduced CeO_2 has been computed to amount to 13.7% [62]. A reduced CeO_2 surface is confirmed by a decreasing ratio. It was 10.2, 9.2, and 11.0 for fresh $Ce_{0.9}Cu_{0.1}O_Y$-cc, cp, and dp, respectively, as shown in Table 2, which indicated that a lot of Ce^{4+} ions were reduced due to the present of Cu. After being reduced by H_2 at 300 °C for 2 h, the value changed depending on the preparation process. It decreased for the $Ce_{0.9}Cu_{0.1}O_Y$-cc and dp samples; however, for the $Ce_{0.9}Cu_{0.1}O_Y$-cp, almost no change was observed. The reduced Ce^{3+} can be reoxidized in air at 300 °C, whereas the oxidation degree did not increase.

Fig. 9a shows the Cu2p XPS spectra of fresh $Ce_{0.9}Cu_{0.1}O_Y$ samples. It can be seen that the fresh $Ce_{0.9}Cu_{0.1}O_Y$-cp catalysts exhibited the Cu 2p3/2 main peak at 933.1 eV. And the fresh $Ce_{0.9}Cu_{0.1}O_Y$-cc and dp showed the Cu 2p3/2 main peak at 932.3 eV. The shake-up satellites at about 942 eV, characteristic for Cu^{2+}, were observed in all the samples, and its intensity was in the order $Ce_{0.9}Cu_{0.1}O_Y$-cp > dp > cc. The degree of reduction can be investigated by determining the ratio of the intensities of the satellite peaks to those of the principal peaks (I_{sat}/I_{pp}). Due to the photoreduction in the spectrometer [63], it is difficult to estimate the accurate degree of reduction, but the method gives valuable information for comparison between catalysts. As shown in Table 2, the intensity ratio of the satellite peak to the corresponding principal peak (I_{sat}/I_{pp}) was found to be 8.7, 13.4, and 9.7%, for $Ce_{0.9}Cu_{0.1}O_Y$-cc, cp, and dp, respectively, which was markedly lower than that of pure CuO (50–60%). Low I_{sat}/I_{pp} values suggested that the CuO_x species should be mainly located in an octahedral coordination environment [64].

Since the BE values and widths for Cu 2p peaks in Cu^+ and Cu^0 are almost identical, the distinction between Cu^+ and Cu^0 species present in the catalyst is only feasible through examination of the Cu-Auger spectra. Fig. 9b shows the kinetic energy spectra of the Auger L_3VV electron. The 915.5 and 917.5 eV peaks in the Auger kinetic spectra correspond to Cu^+ and Cu^{2+} species, respectively [65]. Combined with the Auger spectra and the quantitative calculation results, the Cu 2p3/2 peak at 933.1 eV was ascribed to the overlapping of 933.6 for Cu^{2+} and 932.4 for Cu^+ [66]. So, it was reasonable to suggest that the copper species existed in the form of Cu^{2+} and Cu^+ for the fresh $Ce_{0.9}Cu_{0.1}O_Y$ samples.

Fig. 10a shows the Cu2p XPS spectra of the reoxidized $Ce_{0.9}Cu_{0.1}O_Y$ samples. It can be found that the satellite peak ascribed to the presence of Cu^{2+} recovered and the intensity was higher than that of corresponding fresh samples (Fig. 9a). In the Cu-Auger spectra shown in Fig. 10b, two peaks centered at about 915.5 and 917.5 eV were ob-

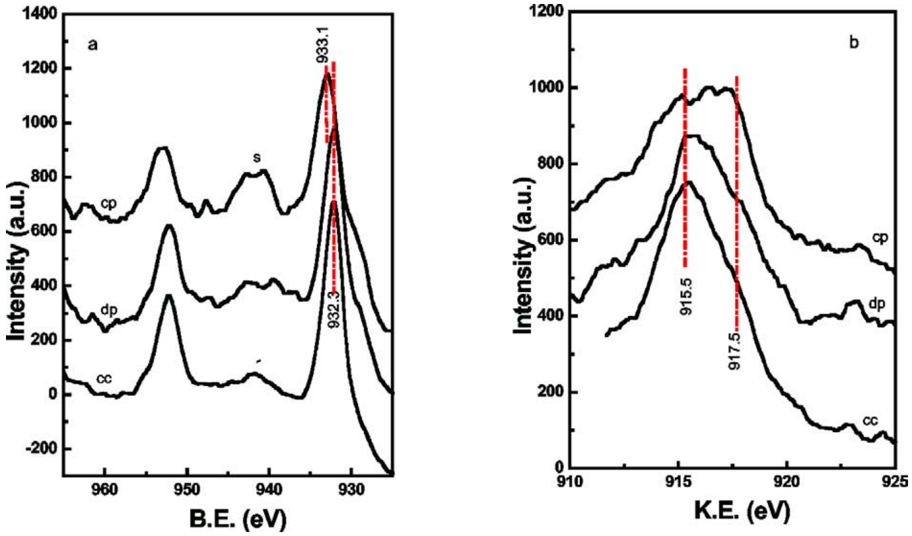

Fig. 9. (a) Cu2p XPS spectra of fresh $Ce_{0.9}Cu_{0.1}O_Y$ samples. (b) CuL3VV spectra of fresh $Ce_{0.9}Cu_{0.1}O_Y$ samples.

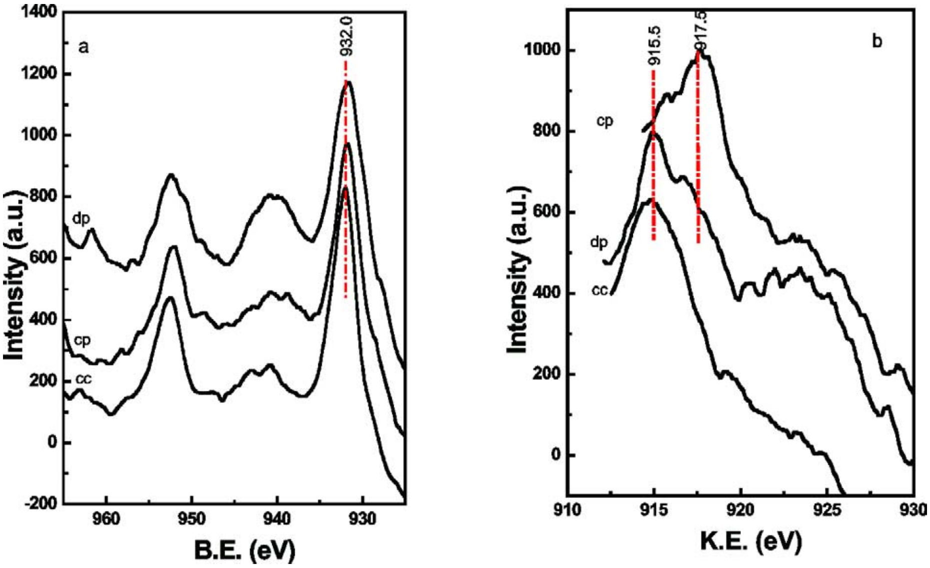

Fig. 10. (a) Cu2p XPS spectra of reoxidated $Ce_{0.9}Cu_{0.1}O_Y$ samples. (b) CuL3VV spectra of reoxidated $Ce_{0.9}Cu_{0.1}O_Y$ samples.

served, which is ascribed to the Cu^+ and Cu^{2+}. Compared with the fresh samples, the $Ce_{0.9}Cu_{0.1}O_Y$-cp showed higher a Cu^{2+} content, whereas almost no change was observed for $Ce_{0.9}Cu_{0.1}O_Y$-cc and $Ce_{0.9}Cu_{0.1}O_Y$-dp.

From XPS results, the structure and redox properties can be understood more clearly. In contrast with dp, the fresh samples cc and cp showed a higher Ce^{4+} reduction degree, which is the reason for the shifting CeO_2 lattice diffraction peak to low 2θ values since the Ce^{3+} (1.03 Å) is larger than Ce^{4+} (0.92 Å). But the Ce^{3+} in the cp and cc showed different changes in the redox cycle. For cp, it was found that the Ce(916.7)/Ce(tot) have no change, although Cu^{2+} can be reduced and reoxidized, which indicated that the Ce^{3+} do not take part in the redox cycle and the reduction of Cu^{2+} is not dependent on the Ce^{4+}/Ce^{3+}couple in this process. Since only the Cu^{2+} takes part in the redox cycle, the H_2 consumption ratio of the reoxidation sample to the corresponding fresh sample at 200–300 °C is about 1.0 as shown in Fig. 7.

In the case of $Ce_{0.9}Cu_{0.1}O_Y$-cc, both Cu^{2+} and Ce^{4+} take part in the redox cycle. The reduced Cu^{2+} can be reoxidized again with the redox of Ce^{4+}/Ce^{3+} couple. It was suggested that the synergistic function between Cu^{2+}/Cu^+ and Ce^{4+}/Ce^{3+} occurred. Comparing the Cu-Auger spectra shown in Fig. 9b and Fig. 10b, it was found that the Cu^{2+} and Cu^+ coexisted for both $Ce_{0.9}Cu_{0.1}O_Y$-cc and $Ce_{0.9}Cu_{0.1}O_Y$-cp due to the $Ce^{4+} + Cu^+ \leftrightarrow Ce^{3+} + Cu^{2+}$ occurring during the calcination process, whereas Cu^+ is the main Cu species for $Ce_{0.9}Cu_{0.1}O_Y$-cc and Cu^{2+} for $Ce_{0.9}Cu_{0.1}O_Y$-cp after the redox cycle. It was suggested that the Cu^+ can be stabilized in $Ce_{0.9}Cu_{0.1}O_Y$-cc due to the formed solid solution. Cu^+ is most easily incorporated into the CeO_2 lattice, considering that the ion radii of Cu^+ (0.96 Å) are similar to Ce^{4+} (0.92 Å) and Ce^{3+} (1.03 Å) and with the same face-centered cubic crystal structure with an octahedral coordination environment. As confirmed in the Raman spectra (Fig. 4), the formation of solid solution produced an increase of oxygen vacancies, which improved the capability of activating and transferring oxygen. Thus, higher redox properties as shown in Fig. 7 were obtained for $Ce_{0.9}Cu_{0.1}O_Y$-cc.

In the $Ce_{0.9}Cu_{0.1}O_Y$-dp sample, CuO dispersed on the surface of CeO_2 which has been calcinated at 450 °C. Although the interaction happened at the interface of CuO and CeO_2, the intrinsical structure of both CuO and CeO_2 has not been changed as confirmed by XRD and Raman spectra. In the redox cycle, some reduced bulk CuO cannot be reoxidized, leading to the low H_2 consumption ratio even at higher reoxidation temperatures as shown in Fig. 7.

3.4. *Oxidative steam reforming of methanol*

The catalytic behaviors for oxidative steam reforming of methanol over $Ce_{0.9}Cu_{0.1}O_Y$ catalysts are compared in Fig. 11. It can be seen that the $Ce_{0.9}Cu_{0.1}O_Y$-cc showed the highest catalytic activity. In the temperature range from 240 to 360 °C, CH_3OH conversion higher than 85% was observed. The $Ce_{0.9}Cu_{0.1}O_Y$-cp and $Ce_{0.9}Cu_{0.1}O_Y$-dp showed low CH_3OH conversion at 240 °C, which is 30 and 25%, respectively. Although, the conversion of CH_3OH increased with increasing the reaction temperature, it is still less than 60% even at 360 °C. The selectivity of CO_2 showed a contrary trend. With the increase of reaction temperatures, the CO_2 decreased. For $Ce_{0.9}Cu_{0.1}O_Y$-cc, the selectivity slightly changed from 97.5% at 240 °C to 90% at 360 °C. The 100% selectivity of CO_2 was observed for $Ce_{0.9}Cu_{0.1}O_Y$-cp and $Ce_{0.9}Cu_{0.1}O_Y$-dp when the reaction temperature was lower than 280 °C. Then it decreased with a further increase in the reaction temperature. Moreover, they exhibited higher CO_2 formation than $Ce_{0.9}Cu_{0.1}O_Y$-cc in the temperature range tested. The dependence of H_2 yield on the reaction temperature showed the same trend as that of CH_3OH conversion for all samples. But, it did not depend on the conversion

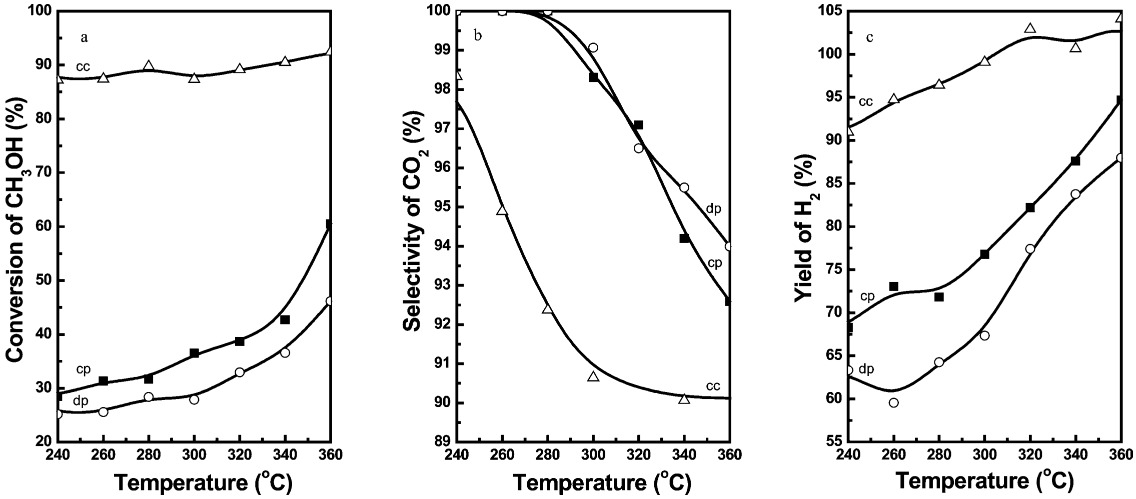

Fig. 11. (a) The conversion of CH_3OH over $Ce_{0.9}Cu_{0.1}O_Y$ catalysts prepared by different methods. (b) The selectivity of CO_2 for OSRM over $Ce_{0.9}Cu_{0.1}O_Y$ catalysts prepared by different methods. (c) The yield of hydrogen for OSRM over $Ce_{0.9}Cu_{0.1}O_Y$ catalysts prepared by different methods.

according the definition of the yield of H_2. The obvious difference in the yield of H_2 indicated that the reaction over the $Ce_{0.9}Cu_{0.1}O_Y$ catalysts followed different pathways depending on preparation methods.

In the combined SRM and POM reaction system, the production of hydrogen from the oxidative steam reforming of methanol involves one or more of the following reactions: partial oxidation (a1), (a2); steam reforming (b); oxidative steam reforming (c); methanol decomposition (d); water–gas shift (e); CO oxidation (f): and H_2 oxidation (g).

$$CH_3OH + \tfrac{1}{4}O_2 \rightarrow 2H_2 + \tfrac{1}{2}CO_2 + \tfrac{1}{2}CO, \tag{a1}$$

$$CH_3OH + \tfrac{1}{2}O_2 \rightarrow 2H_2 + CO_2, \tag{a2}$$

$$CH_3OH + H_2O \rightarrow 3H_2 + CO_2, \tag{b}$$

$$CH_3OH + (1-2\delta)H_2O + \delta O_2 \rightarrow (3-2\delta)H_2 + CO_2, \tag{c}$$

$$CH_3OH \rightarrow 2H_2 + CO, \tag{d}$$

$$CO + H_2O \Leftrightarrow H_2 + CO_2, \tag{e}$$

$$CO + \tfrac{1}{2}O_2 \rightarrow CO_2, \tag{f}$$

$$H_2 + \tfrac{1}{2}O_2 \rightarrow H_2O. \tag{g}$$

The higher reaction temperature promoted the endothermic reactions (b) and (d), which was the reason for the low selectivity of CO_2 and the high yield of H_2 at high temperatures ($> 300\,°C$). According to the definition, the high yield of H_2 indicated a higher selectivity to proceed OSRM than other reactions. For $Ce_{0.9}Cu_{0.1}O_Y$-cc, the yield of H_2 higher than 91% was observed, which means that the oxidative steam reforming of methanol was primary, although the consumption hydrogen reactions occurred, such as hydrogen oxidation and reversible water–gas shift. While, the yields of H_2 over $Ce_{0.9}Cu_{0.1}O_Y$-cp and $Ce_{0.9}Cu_{0.1}O_Y$-dp were not higher than 75% at temperatures $< 300\,°C$, suggesting that hydrogen production on these catalysts followed some low hydrogen production reactions (a1), (a2), and (d), or some consumption hydrogen reactions performed to a significant degree. Considering the high selectivity of CO_2, the reversible water–gas shift reaction was not the major H_2 consumption reaction. Therefore, a process consisting of the oxidation of CO and H_2 following the partial oxidation and the decomposition of methanol may play important roles for the $Ce_{0.9}Cu_{0.1}O_Y$-cp and $Ce_{0.9}Cu_{0.1}O_Y$-dp catalysts.

So it can be concluded that the $Ce_{0.9}Cu_{0.1}O_Y$-cp and $Ce_{0.9}Cu_{0.1}O_Y$-dp samples not only showed low activity for hydrogen production from methanol but also enhanced the conversion of produced H_2, resulting in both lower methanol conversions and lower H_2 selectivity. On the contrary, the $Ce_{0.9}Cu_{0.1}O_Y$-cc showed high activity and selectivity for OSRM. Based on the characterization results described above, it seems that the catalytic activity is related to the solid solution structure and the higher redox properties. The $Ce_{0.9}Cu_{0.1}O_Y$-cc catalyst could be a promising catalyst for the production of hydrogen from methanol.

4. Conclusion

The structural properties as well as the catalytic behaviors of the $Ce_{0.9}Cu_{0.1}O_Y$ catalyst strongly depend on the preparation routes. The XRD and Raman results indicated that the solid solution forms in the $Ce_{0.9}Cu_{0.1}O_Y$ catalyst prepared by the complexation–combustion method, which enhances the defects of CeO_2, corresponding to the stoichiometric composition of $CeO_{2-\delta}$ due to Cu^{2+} incorporated in CeO_2 lattice. The formation of a solid solution structure also lowers the reduction temperature of $Ce_{0.9}Cu_{0.1}O_Y$ and improves the redox properties, which is ascribed to the synergistic function between Cu^{2+}/Cu^{+} and Ce^{4+}/Ce^{3+} occurring in the redox cycle as shown in the XPS spectra. Consequently, high catalytic activity in the oxidative steam reforming of methanol was observed. However, the $Ce_{0.9}Cu_{0.1}O_Y$-cp and

$Ce_{0.9}Cu_{0.1}O_Y$-dp show lower conversions of CH_3OH and yield of H_2, although relatively higher selectivity of CO_2 was observed. It seemed that the redox properties of catalyst affect the catalytic activity and H_2 production pathway for the oxidative steam reforming of methanol.

References

[1] X.R. Zhang, P. Shi, J. Zhao, M. Zhao, C. Liu, Fuel Process. Technol. 83 (2003) 183.
[2] Ya-Huei Chin, Y. Wang, R.A. Dagle, X.S. Li, Fuel Process. Technol. 83 (2003) 193.
[3] J. Agrell, H. Birgersson, M. Boutonnet, I. Meliän-Cabrera, R.M. Navarro, J.L.G. Fierro, J. Catal. 219 (2003) 389.
[4] N. Iwasa, S. Masuda, N. Ogawa, N. Takezawa, Appl. Catal. A 125 (1995) 145.
[5] B. Lindström, J. Agrell, L.J. Pettersson, J. Chem. Eng. 93 (2003) 91.
[6] X. Zhang, P. Shi, J. Mol. Catal. A: Chem. 194 (2003) 99.
[7] D.F. Löffler, S.D. McDermott, C.N. Renn, J. Power Sources 114 (2003) 15.
[8] J. Agrell, G. Germani, Sven G. Järås, M. Boutonnet, Appl. Catal. A 242 (2003) 233.
[9] Y. Choi, H.G. Stenger, Appl. Catal. B 38 (2002) 259.
[10] S.R. Segal, K.B. Anderson, K.A. Carrado, C.L. Marshall, Appl. Catal. A 231 (2002) 215.
[11] A.P. Tsai, M. Yoshimura, Appl. Catal. A 214 (2001) 237.
[12] L. Alejo, R. Lago, M.A. Peña, J.L.G. Fierro, Appl. Catal. A 162 (1997) 281.
[13] S. Velu, K. Suzuki, M.P. Kapoor, F. Ohashi, T. Osaki, Appl. Catal. A 213 (2001) 47.
[14] B. Lindström, L.J. Pettersson, P.G. Menon, Appl. Catal. A 234 (2002) 111.
[15] S. Murcia-Mascarós, R.M. Navarro, L. Gómez-Sainero, U. Costantino, M. Nocchetti, J.L.G. Fierro, J. Catal. 198 (2001) 338.
[16] S. Velu, K. Suzuki, T. Osaki, Chem. Commun. (1999) 2341.
[17] R. Kumar, S. Ahmed, M. Krumpelt, K. M. Myles, US patent 5,248,566 (1993).
[18] S. Ahmed, M. Krumpelt, Int. J. Hydrogen Energy 26 (2001) 291.
[19] T.L. Reitz, S. Ahmed, M. Krumpelt, R. Kumar, H.H. Kung, J. Mol. Catal. 162 (2000) 275.
[20] T.L. Reitz, P.L. Lee, K.F. Czaplewski, J.C. Lang, K.E. Popp, H.H. Kung, J. Catal. 199 (2001) 193.
[21] S. Velu, K. Suzuri, M. Okazaki, M.P. Kapoor, T. Osaki, D. Ohashi, J. Catal. 194 (2000) 373.
[22] B. Lindström, L.J. Pettersson, P.G. Menon, Appl. Catal. A 234 (2002) 111.
[23] I.A. Fisher, A.T. Bell, J. Catal. 172 (1997) 222.
[24] I.A. Fisher, A.T. Bell, J. Catal. 178 (1998) 153.
[25] I.A. Fisher, A.T. Bell, J. Catal. 184 (1999) 357.
[26] J.A. Rodriguez, J.Y. Kim, J.C. Hanson, M. Pérez, A.I. Frenkel, Catal. Lett. 85 (2003) 247.
[27] L. Li, G. Li, Y. Che, W. Su, Chem. Mater. 12 (2000) 2567.
[28] A. Bensalem, F. Bozon Verduraz, M. Delamar, G. Bugli, Appl. Catal. 121 (1995) 81.
[29] R.K. Usman, G.W. Graham, W.L.H. Watkins, R.W. McCabe, Catal. Lett. 30 (1995) 53.
[30] F. Zamar, A. Trovarelli, C. De Leitenburg, G. Dolcetti, J. Chem. Soc., Chem. Commum. (1995) 965.
[31] M. Luo, J. Chen, J. Lu, Z. Feng, C. Li, Chem. Mater. 13 (2001) 1491.
[32] A.I. Kozlov, D.H. Kim, A. Yezerets, P. Andersen, H.H. Kung, M.C. Kung, J. Catal. 209 (2002) 417.
[33] N. Sergent, J. Lamonier, A. Aboukaïs, Chem. Mater. 12 (2000) 3830.
[34] P. Bera, K.R. Priolkar, P.R. Sarode, M.S. Hegde, S. Emura, R. Kumashiro, N.P. Lalla, Chem. Mater. 14 (2002) 3591.
[35] P. Bera, K.R. Priolkar, A. Gayen, P.R. Sarode, M.S. Hegde, S. Emura, R. Kumashiro, V. Yayaram, G.N. Subbanna, Chem. Mater. 15 (2003) 2049.
[36] K.R. Priolkar, P. Bera, A. Gayen, P.R. Sarode, M.S. Hegde, S. Emura, R. Kumashiro, N.P. Lalla, Chem. Mater. 14 (2002) 2120.
[37] P. Bera, S.T. Aruna, K.C. Patil, M.S. Hegde, J. Catal. 186 (1999) 36.
[38] S. Hočevar, J. Batista, J. Levec, J. Catal. 184 (1999) 39.
[39] W. Liu, M. Flytzani-Stephanopoulos, J. Catal. 153 (1995) 304.
[40] A. Martínez-Arias, M. Fernández-García, O. Gálvez, J.M. Coronado, J.A. Anderson, J.C. Conesa, J. Soria, G. Munuera, J. Catal. 195 (2000) 207.
[41] P. Bera, S. Mitra, S. Sampath, M.S. Hegde, Chem. Commun. (2001) 927.
[42] B. Skårman, T. Nakayama, D. Grandjean, R.E. Benfield, K. Olsson, K. Niihara, L.R. Wallenberg, Chem. Mater. 14 (2002) 3686.
[43] D.H. Tsai, T.J. Huang, Appl. Catal. A 223 (2002) 1.
[44] P.G. Harrison, I.K. Ball, W. Azelee, W. Daniell, D. Goldfarb, Chem. Mater. 12 (2000) 3715.
[45] B. Skårman, D. Grandjean, R.E. Benfield, A. Hinz, A. Andersson, L.R. Wallenberg, J. Catal. 211 (2002) 119.
[46] G. Sedmak, S. Hočevar, J. Levec, J. Catal. 213 (2003) 135.
[47] G. Avgouropoulos, T. Ioannides, Ch. Papadopoulou, J. Batista, S. Hocevar, H.K. Matralis, Catal. Today. 75 (2002) 157.
[48] G. Avgouropoulos, T. Ioannides, H.K. Matralis, J. Batista, S. Hocevar, Catal. Lett. 73 (1) (2001) 33.
[49] Y. Li, Q. Fu, M. Flytzani-Stephanopoulos, Appl. Catal. B 27 (2000) 179.
[50] Y. Liu, T. Hayakawa, K. Suzuki, S. Hamakawa, T. Tsunoda, T. Ishii, M. Kumagai, Appl. Catal. A 223 (2002) 137.
[51] W.J. Shan, W.J. Shen, C. Li, Chem. Mater. 15 (2003) 4761.
[52] G. Adachi, N. Imanaka, Chem. Rev. 98 (1998) 1479.
[53] Y. Zhang, S. Andersson, M. Muhammed, Appl. Catal. B: Env. 6 (1995) 325.
[54] A Trovarelli (Ed.), Catalysis by Ceria and Related Materials, Università di Udine, Italy, Imperial College Press.
[55] D.L. Bhering, M. Nele, J.C. Pinto, V.M.M. Salim, Appl. Catal. A 234 (2002) 55.
[56] M. Kakihana, J. Sol–Gel Sci. Technol. 6 (1996) 7.
[57] H.P. Klug, L.E. Alexander, X-Ray Diffraction Procedures, Wiley, New York, 1954.
[58] B.M. Reddy, A. Khan, Y. Yamada, T. Kobayashi, S. Loridant, J.-C. Volta, J. Phys. Chem. B 107 (41) (2003) 11475.
[59] J.E. Spanier, R.D. Robinson, F. Zhang, S.W. Chan, I.P. Herman, Phys. Rev. B 64 (2001) 245407.
[60] J.R. McBride, K.C. Hass, B.D. Poindexter, W.H. Weber, J. Appl. Phys. 76 (1994) 2435.
[61] P. Zimmer, A. Tschöpe, R. Birringer, J. Catal. 205 (2002) 339.
[62] J.Z. Shyu, W.H. Weber, H.S. Gandhi, J. Phys. Chem. 92 (1988) 4964.
[63] P.-O. Larsson, A. Andersson, L.R. Wallenberg, B. Svensson, J. Catal. 163 (1996) 279.
[64] S. Bennici, A. Gervasini, N. Ravasio, F. Zaccheria, J. Phys. Chem. B 107 (2003) 5168.
[65] W. Liu, M. Flytzani-Stephanopoulos, J. Catal. 153 (1995) 317.
[66] S. Velu, Kenzi Suzuki, J. Phys. Chem. B 106 (2002) 12737.